UC Irvine

UC Irvine Previously Published Works

Title

Silver content dependent thermal conductivity and thermoelectric properties of electrodeposited antimony telluride thin films

Permalink

https://escholarship.org/uc/item/3gg7t0fk

Journal

Scientific Reports, 9(1)

ISSN

2045-2322

Authors

Ferrer-Argemi, Laia
Yu, Ziqi
Kim, Jiwon
et al.

Publication Date

2019

DOI

10.1038/s41598-019-45697-9

Copyright Information

This work is made available under the terms of a Creative Commons Attribution License, availalbe at https://creativecommons.org/licenses/by/4.0/

Peer reviewed

eScholarship.org Powered by the California Digital Library
University of California

SCIENTIFIC REPORTS

OPEN

Silver content dependent thermal conductivity and thermoelectric properties of electrodeposited antimony telluride thin films

Received: 8 October 2018
Accepted: 13 June 2019
Published online: 25 June 2019

Laia Ferrer-Argemi[1], Ziqi Yu[1], Jiwon Kim[2], Nosang V. Myung[3], Jae-Hong Lim[4] & Jaeho Lee[1]

While electrodeposited antimony telluride thin films with silver contents demonstrated promising thermoelectric properties, their thermal conductivity and the silver content dependence remain unknown. Here, we report the thermal conductivities of $Ag_{3.9}Sb_{33.6}Te_{62.5}$ and $AgSbTe_2$ thin films with controlled annealing and temperature conditions and demonstrate the impact of silver content on thermal transport. After annealing at 160 °C, the room-temperature thermal conductivity of $Ag_{3.9}Sb_{33.6}Te_{62.5}$ and $AgSbTe_2$ thin films increases from 0.24 to 1.59 $Wm^{-1}K^{-1}$ and from 0.17 to 0.56 $Wm^{-1}K^{-1}$, respectively. Using phonon transport models and X-ray diffraction measurements, we attribute the thermal conductivity increases to the crystal growth and explain the thermal conductivity variations with the degree of crystallization. Unlike electrical properties reported in previous studies, the presence of silver contents has little impact on the thermal conductivity of $Ag_{3.9}Sb_{33.6}Te_{62.5}$ and leads to a strong reduction in the thermal conductivity of $AgSbTe_2$ thin films. By performing transient thermal conductivity measurements at 94 °C, we find the crystallization activation energy of $Ag_{3.9}Sb_{33.6}Te_{62.5}$ and $AgSbTe_2$ films as 1.14 eV and 1.16 eV, respectively. Their differences reveal the role of silver in inhibiting the nucleation and growth of Sb_2Te_3 crystals and impeding thermal transport. These findings provide guidance for optimizing doping and annealing conditions of antimony tellurides for near-room-temperature thermoelectric applications.

Nanostructured thermoelectric (TE) materials are widely studied for reducing the thermal conductivity and improving the power factor, which can increase the efficiency of thermoelectric power generators and solid-state cooling devices[1–5]. While fabrication of nanostructures often requires expensive and non-scalable processes, an electrodeposition technique provides combined attributes of cost-effectiveness, scalability, and precise control over crystallinity and composition[6–8]. Electrodeposition is thus ideal for studying the effects of crystal size and film composition, including doping concentration, in thermoelectric materials. Including dopants to the material composition has been proven to be an effective strategy to improve the thermoelectric figure of merit (zT) of chalcogenide semiconductors such as PbTe[9], SnSb[10], SnSe[5], and $AgSbTe_2$[11]. Doping can increase the electrical conductivity σ and have varying results on other properties. While low doping concentrations reduce the thermal conductivity κ and increase the Seebeck coefficient S, larger doping concentrations reduce the Seebeck coefficient and increase the thermal conductivity[1]. Yamashita *et al.*[12] doped different antimony telluride compounds with tellurium excess to obtain p-type and n-type thermoelectric materials with a zT of 1.41 and 1.13, respectively. Mehta *et al.*[13] measured an improved Sb_2Te_3 zT of 0.95 using sulfur doping and theoretically show that a maximum of 2 could be reached by doping optimization.

Among the antimony telluride material family, bulk $AgSbTe_2$ has demonstrated an extremely low lattice thermal conductivity of 0.7 $Wm^{-1}K^{-1}$ [14], which has been attributed to phonon scattering with heterophases[15] and the

[1]Department of Mechanical and Aerospace Engineering, University of California, Irvine, Irvine, CA, 92697, USA. [2]Electrochemistry Research Group, Materials Processing Division, Korea Institute of Materials Science, Changwon-si, Gyeongnam, 51508, Republic of Korea. [3]Department of Chemical and Environmental Engineering and UC-KIMS CIME, University of California-Riverside, Riverside, California, 92521, USA. [4]Department of Materials Science and Engineering, Gachon University, Seongnam, 13120, Republic of Korea. Correspondence and requests for materials should be addressed to J.-H.L. (email: limjh@gachon.ac.kr) or J.L. (email: jaeholee@uci.edu)

formation of nanoscale cation sublattices[16]. Du *et al.*[11] reached a zT of 1.4 at 550 K after doping $AgSbTe_2$ with 2% Se. Concentrations of silver lower than the stoichiometry can produce impurities in the matrix or form precipitates, both of which are favorable to reduce the thermal conductivity[17,18]. In particular, Sb_2Te_3/Ag_2Te composites fabricated using ball milling have been found to improve the zT up to 1.5 at 700 K, and $AgSbTe_2/Ag_2Te$ quenched ingots reached 1.5 at 500 K[19]. Besides the material composition and doping, the morphology is been shown to be a key parameter in the resulting thermoelectric properties. For instance, our previous studies[6,8] demonstrated a zT of 0.35 for electrodeposited $Sb_{37}Te_{63}$ films pre-annealed at 80 °C due to the combination of low thermal conductivity and enhanced power factor provided by a secondary phase; and nanostructured $Bi_{0.5}Sb_{1.5}Te_3$ achieved a zT above 1 at room temperature by inducing small grain sizes and highly dense dislocations[20,21].

Our recent studies reported the power factor of antimony telluride electrodeposited thin films with silver content from 0 to 30% and annealing temperatures up to 100 °C[7,22]. Among the studied electrodeposited thin films, the highest power factor (1870 $\mu Wm^{-1}K$) was obtained in $Ag_{3.9}Sb_{33.6}Te_{62.5}$ due to the Ag doping of the Sb_2Te_3 matrix and the presence of β-$AgTe_2$ nanoprecipitates (~6% in vol.) that were formed after annealing at 100 °C[7]. Electrodeposited $AgSbTe_2$ annealed at 100 °C also demonstrated a high power factor of 553 $\mu Wm^{-1}K$ and it is expected to present a very low thermal conductivity that could lead to higher zT values[14]. These power factors indicate promising materials for thermoelectric applications, which motivated a more detailed study of the thermal properties of the electrodeposited films with different compositions and annealing conditions. We report the thermal conductivity measurements of electrodeposited $Ag_{3.9}Sb_{33.6}Te_{62.5}$ and $AgSbTe_2$ thin films as a function of their pre-annealing temperature, annealing time, and measurement temperature. By comparing the thermal conductivity of SbTe films with varying silver contents and by analyzing the temperature- and time-dependent thermal conductivity data, this work provides a detailed understanding of the effects of silver content and crystallization on thermal transport.

Results and Discussion

The morphology and thickness of the electrodeposited $AgSbTe_2$ and $Ag_{3.9}Sb_{33.6}Te_{62.5}$ films are examined by Scanning Electron Microscopy (SEM) (Quanta, Thermo Scientific™) imaging. Figure 1(b) displays a cross-sectional SEM image of a measured $AgSbTe_2$ film where we can identify, from top to bottom, the Ni/Cr electrode, the SiO_2 passivation layer, the $AgSbTe_2$ film, and the Au/Ti/SiO_2/Si stack. The thickness of the $AgSbTe_2$ films in our work ranges from 300 to 500 nm and the thickness of the $Ag_{3.9}Sb_{33.6}Te_{62.5}$ films (Fig. 1(c)) ranges from 0.6 to 1 μm, all with compact and smooth morphology. The crystallinity and the phase transformation of $AgSbTe_2$ and $Ag_{3.9}Sb_{33.6}Te_{62.5}$ films are investigated by X-ray Diffraction (XRD) (Smartlab, Rigaku Corp™) analysis and the average grain size is estimated based on the major XRD peaks. Our previous studies confirmed the stoichiometry crystallization of $AgSbTe_2$ in the Ag-rich film[22], and the formation of β-Ag_2Te (~6% in vol.) nanoprecipitates and a silver-doped Sb_2Te_3 matrix in the Ag-deficient film upon annealing at 100 °C[7]. In Fig. 1(d), XRD spectra of $Ag_{3.9}Sb_{33.6}Te_{62.5}$ films pre-annealed at different temperatures shows a rapid Sb_2Te_3 crystallization (JCPDS 15-0874) after annealing at temperatures above 85 °C, reaching an average grain size of 26 nm after annealing at 133 °C. Detailed information on XRD spectra can be found in the Supplementary Note 1. The average grain size is estimated using the Debye-Scherrer equation and detailed in Fig. 1(e) as $D = \frac{k\lambda}{FWHM \cdot \cos\theta}$, where k is a shape factor whose value usually takes 0.9, λ is the X-ray wavelength of 1.54 Å, FWHM is the full-width-half-maximum obtained by analyzing XRD peaks, and θ is the Bragg angle. Peaks attributed to slightly deficient antimony telluride appears after annealing at 133 °C ($Sb_{0.405}Te_{0.595}$: JCPDS 45-1229) due to the precipitation of β-Ag_2Te.

Figure 2 shows the effective thermal conductivity κ as a function of the pre-annealing temperature, see the Methods section for details of the measurement technique. We observe a monotonic increase in the thermal conductivity of $AgSbTe_2$ films which indicates increasing crystallization and larger phonon mean free paths; and, while $Ag_{3.9}Sb_{33.6}Te_{62.5}$ films present only a slightly higher thermal conductivity at pre-annealing temperatures below 90 °C, a sudden increase occurs when Sb_2Te_3 starts to crystallize and reaches the same thermal conductivity as the $Sb_{37}Te_{63}$ reported in our previous study[8]. This indicates that the silver doping delays the crystallization of Sb_2Te_3, providing a lower thermal conductivity at pre-annealing temperatures below 100 °C and that, unlike reported in previous studies of Sb_2Te_3 films[23], the electron thermal conductivity does not contribute significantly to the total thermal conductivity of $Ag_{3.9}Sb_{33.6}Te_{62.5}$ films which are 50 times more electrically conductive than $Sb_{37}Te_{63}$ films[6,7]. The overall lower thermal conductivity of the $AgSbTe_2$ films is as expected because of the extremely low thermal conductivity of bulk $AgSbTe_2$ (0.7 $Wm^{-1}K^{-1}$) due to the strong anharmonicity of its bonding arrangement[24]. The main uncertainty of the thermal conductivity measured the 3ω method comes from the fitting of the temperature coefficient of resistance (TCR) to the measured resistance change with temperature, which is required for extracting the information about the thermal conductivity from the measured electrical data by matching the temperature rise with theoretical prediction given by the solution to the multilayer conduction equation. Although the resistance of the metal line is measured with a maximum uncertainty of 0.3% for the less resistive metal lines, and the placement of a platinum RTD sensor on the sample holder provides a more accurate temperature measurement with 2% uncertainty, the linear fit of the change of the resistance with temperature (dR/dT) leads to an uncertainty of up to 5%[25]. The TCR was first measured after annealing the sample at 70 °C and then another TCR was measured after annealing at higher temperatures. The TCR was consistent among samples ($TCR_1 = 0.005 \pm 0.0002K^{-1}$) with the same annealing history, and no variations are expected before that because the resistance of the heater line at room temperature was constant. Another major uncertainty in our measurement is the thickness of the film, in which the contribution was minimized by performing cross-sectional SEM images. The film thicknesses were found to be constant within 10% in the measurement region as seen in Fig. 1. With the differential measurement, the only other uncertainty comes from the 3ω reading and fitting. The use of lock-in amplifier ensures accurate in-phase measurements within 0.5% and the fitting algorithm provides the best fit of the thermal conductivity down to 0.002 $Wm^{-1}K^{-1}$. Overall, this results in an uncertainty between 15 and 20% for the highest and lowest thermal conductivity values, respectively. Using the power factors that we

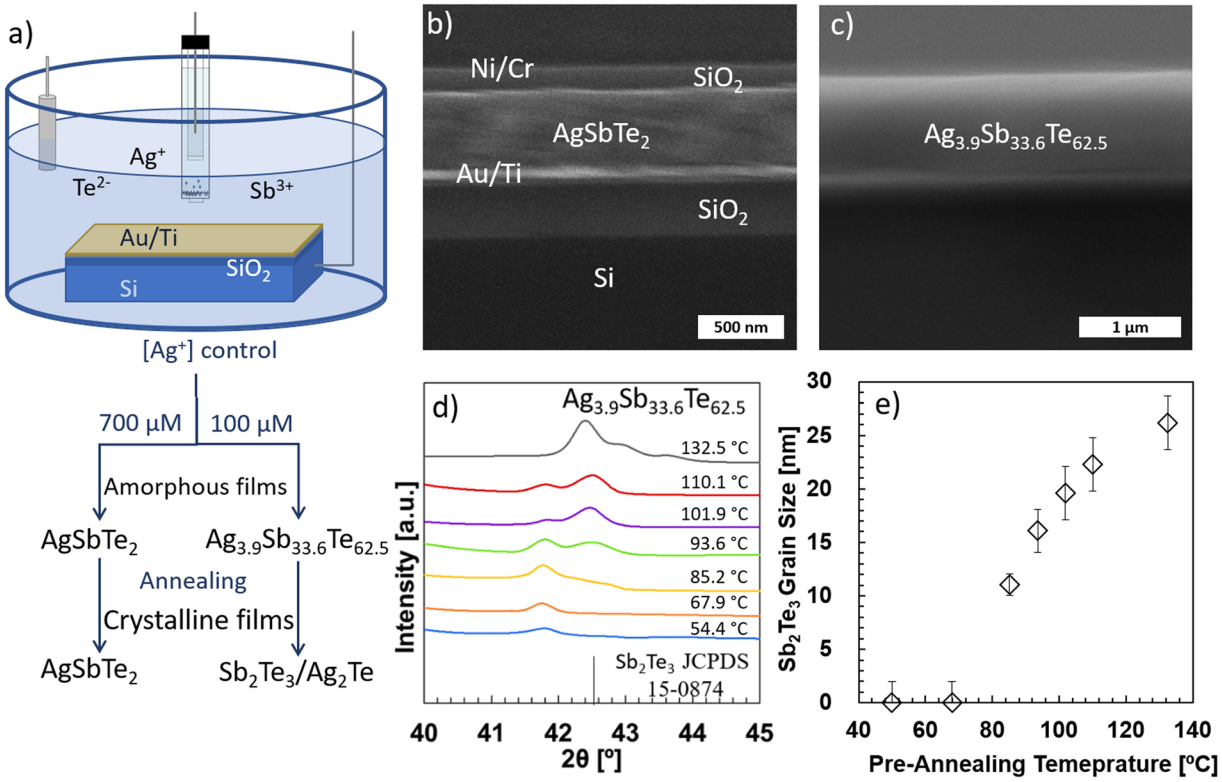

Figure 1. (**a**) Schematic of the sample fabrication by potentiostatic electrodeposition and control of the Ag^+ concentration. The electrolytic exact composition can be found in our previous publications[7,22]. The amorphous electrodeposited films can be annealed at different temperatures to tune their thermoelectrical properties. A passivation layer (SiO_2) and Ni/Cr electrodes are fabricated using e-beam deposition and photolithography[8]. Representative cross-sectional SEM images of measured $AgSbTe_2$ (**b**) and $Ag_{3.9}Sb_{33.6}Te_{62.5}$ (**e**) films. The thicknesses of the labeled layers of the Ni/Cr/SiO_2/film/Au/Ti/SiO_2/Si stack are 100 nm, 20 nm, 150 nm, 0.3–1 µm, 50 nm, 30 nm, 300 nm, and 500 µm, respectively. The $AgSbTe_2$ film thickness ranged from 300 to 500 nm and the $Ag_{3.9}Sb_{33.6}Te_{62.5}$ ranged from 600 to 1000 nm in our study. The fabrication processes are carefully controlled to keep the temperature below 50 °C and avoid any crystallization. (**c**) X-ray diffraction (XRD) data of an electrodeposited $Ag_{3.9}Sb_{33.6}Te_{62.5}$ film after being annealed at 50, 68, 85, 94, 102, and 133 °C on a hot plate in vacuum for 30 minutes. Rhombohedral Sb_2Te_3 dominates the crystallization after annealing at 85 °C. $AgSbTe_2$ films monotonically increase their crystal size with annealing temperature. (**d**) Average grain size of Sb_2Te_3 in $Ag_{3.9}Sb_{33.6}Te_{62.5}$ films based on the XRD peak broadening, as estimated by the Debye-Scherrer equation.

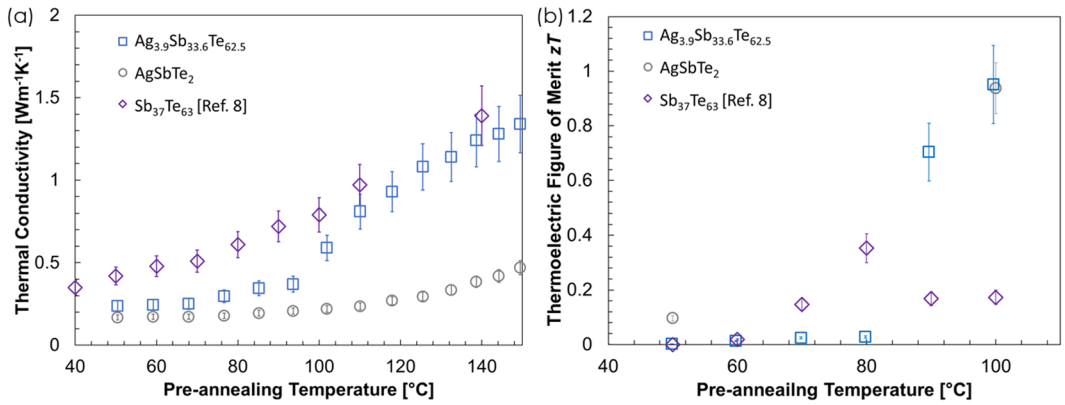

Figure 2. (**a**) Thermal conductivity of $Ag_{3.9}Sb_{33.6}Te_{62.5}$ (blue square), and $AgSbTe_2$ (grey circle) films measured using the 3ω method after annealing for 30 minutes in vacuum at different temperatures. The increasing trend is attributed to the increase in the films crystallinity and grain size as indicated by the XRD data. (**b**) Predicted thermoelectric figure of merit after annealing for 30 minutes. The power factor used in zT calculations is taken from our previous publications[7,22]. Our previous data on $Sb_{37}Te_{63}$ (purple diamonds) is also shown for comparison[8].

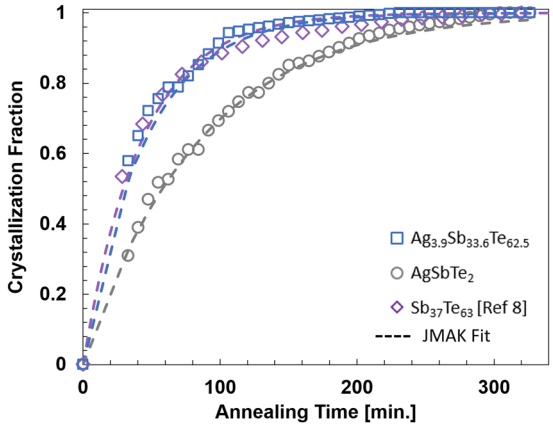

Figure 3. Crystallization fraction of $Ag_{3.9}Sb_{33.6}Te_{62.5}$ (blue square) and $AgSbTe_2$ (grey circle) films based on the thermal conductivity data as a function of annealing time at 94 °C. Data of $Sb_{37}Te_{63}$ (purple diamonds) from Yu *et al.* is also shown for comparison[8]. The data is fitted using the JMAK model (dashed lines) where the activation energy (1.14 eV for $Ag_{3.9}Sb_{33.6}Te_{62.5}$ and 1.16 eV for $AgSbTe_2$) and the Avrami constant (n = 1) are obtained by the best fit to the experimental data.

measured after different pre-annealing temperatures for samples of the same batch and reported in our previous work (i.e. 2.3 and 0.14 $\mu Wm^{-1}K^{-2}$ after annealing at 50 °C, and 1870 and 553 $\mu Wm^{-1}K^{-2}$ after annealing at 100 °C for $Ag_{3.9}Sb_{33.6}Te_{62.5}$ and $AgSbTe_2$ films, respectively)[7,22], we obtain a maximum zT value at room temperature of 0.95 ± 0.17 for $Ag_{3.9}Sb_{33.6}Te_{62.5}$ and 0.93 ± 0.10 for $AgSbTe_2$ electrodeposited films after annealing at 100 °C. For details on the zT calculation, see Supplementary Note 2. The predicted zT values are among the highest reported to date among nanostructured bulk $AgSbTe_2$[20,26–29], further experimentation is required to optimize the zT with slightly different pre-annealing temperatures around 100 °C.

In order to compare the crystallization dynamics of $AgSbTe_2$ and $Ag_{3.9}Sb_{33.6}Te_{62.5}$ films, we measured the thermal conductivity during a 5.5-hour annealing at 94 °C. We convert the time-dependent thermal conductivity data into crystallization fraction by assuming that the amorphous regions are uniformly distributed across the film and in parallel with the crystallized regions, which is equivalent to assuming the columnar grain growth reported for other SbTe-based films[25]. Defining the stationary thermal conductivity reached at the end of the annealing process as crystalline thermal conductivity κ_c at the measured temperature and the amorphous thermal conductivity κ_a as the initial one, we can compute the crystalline fraction x_c from

$$\kappa_{eff} = x_c\kappa_c + (1 - x_c)\kappa_a, \quad (1)$$

where κ_z is the effective cross-sectional thermal conductivity measured at each time step. The use of Eq. (1) for the volume fraction calculation assumes that the crystallized regions are uniformly distributed across the film in parallel with the amorphous regions. This is a reasonable assumption for films that have a columnar growth of crystalline regions upon thermal annealing[25]. Other effective medium theory models[30–35] could be used with different assumptions on the crystalline phase distribution, but the change in volume fraction calculation is expected to be small. For instance, the use of another EMT assuming crystallized regions are distributed in series with amorphous regions results in a difference in the volume fraction calculation less than 0.046 for the transient thermal conductivity measurements performed in this work. In Fig. 3, we compare the crystallization fraction calculated from the experimental data with that predicted by the Johnson-Mehl-Avrami-Kolmogorov (JMAK) equation. The JMAK model[36] relates the crystallization fraction with the crystallization activation energy ΔH and the time as $x_c = \exp(-k_p t^n)$, where $k_p = exp\left(-k_0\frac{\Delta H}{k_B T}\right)$, n is the Avrami number, k_0 is the crystallization constant, and k_B is the Boltzmann constant. We find a crystallization constant of 10^{15}, a crystallization activation energy of 1.142 eV for $Ag_{3.9}Sb_{33.6}Te_{62.5}$ films and 1.162 eV for $AgSbTe_2$ films, and the Avrami number of 1, which indicates that the phase transformation process is governed by one-dimensional interface-controlled nucleation growth. The activation energy obtained for $Ag_{3.9}Sb_{33.6}Te_{62.5}$ films coincides with the previously reported for $Sb_{37}Te_{63}$ films, which confirms the nucleation of Sb_2Te_3 and indicates that the creation of nanoprecipitates does not affect the crystallization rate. On the contrary, the activation energy required to crystallize $AgSbTe_2$ is found to be slightly higher, which increases the annealing time required to achieve full crystallization and might be the reason why the crystallization of Sb_2Te_3 requires higher temperatures in the lightly silver doped films than in the previously studied $Sb_{37}Te_{63}$ films.

To confirm the crystalline nature of $AgSbTe_2$ and $Ag_{3.9}Sb_{33.6}Te_{62.5}$ films under different annealing conditions, we measured the temperature-dependent thermal conductivity of the films up to the pre-annealing temperature. The results, shown in Fig. 4, clearly show different temperature dependences after the films are annealed at different temperatures. The thermal conductivity of $Ag_{3.9}Sb_{33.6}Te_{62.5}$ pre-annealed at 70 °C shows the typical behavior of a highly disordered amorphous material: an almost constant low value with a slight increase with temperature because of the thermal activation of thermal carriers with very short phonon average mean free path[37,38]. This

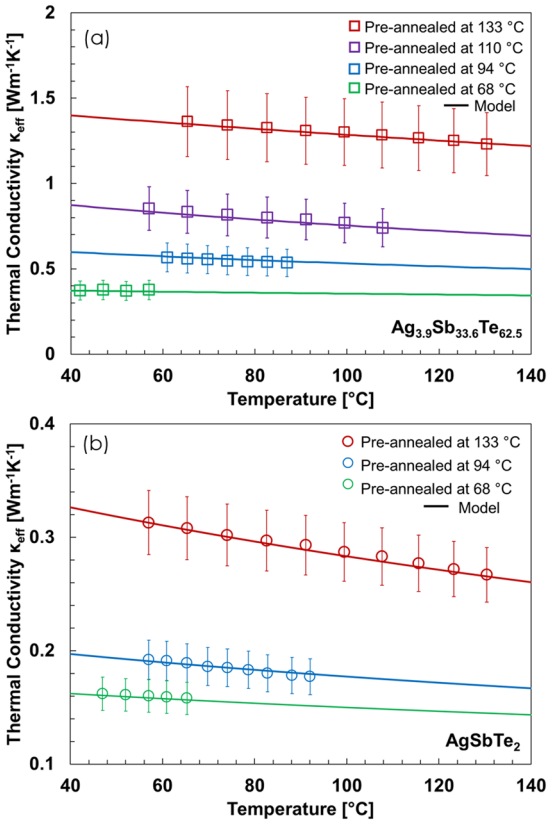

Figure 4. Thermal conductivity as a function of the measurement temperature for (**a**) $Ag_{3.9}Sb_{33.6}Te_{62.5}$ and (**b**) $AgSbTe_2$ films after being annealed at different pre-annealing temperatures. We use a combination of the Callaway model[44] and the Einstein model[39] to fit the thermal conductivity of the crystalline and amorphous phases, respectively. While Umklapp scattering behavior dominates after annealing at 133 °C due to the short phonon mean path of the Sb_2Te_3 and $AgSbTe_2$ films, the weak temperature dependence of the films annealed at temperatures below 100 °C indicates a competing effect between amorphous and crystalline phases.

trend can be supported by the modified Einstein model[39], where a minimum thermal conductivity is described as the random walk of phonons through lattices and it is expressed as

$$\kappa_a = \left(\frac{\pi}{6}\right)^{1/3} k_B n^{2/3} \sum_i v_g \left(\frac{T}{\Theta_D}\right)^2 \int_0^{\Theta_i/T} \frac{x^3 e^x}{(e^x - 1)^2} dx, \tag{2}$$

where n is the atomic number density, the sum is taken over one longitudinal and two-transverse modes, v_g is the average sound velocity, T is the temperature of the film, and Θ_D is the Debye temperature for each mode. For $AgSbTe_2$, the average sound speed, atomic number density, and Debye temperature are 1490 ms^{-1}, $3.57 \times 10^{28}\, m^{-3}$, and 150 K, respectively[40,41]. Due to the low volume fraction of Ag in $Ag_{3.9}Sb_{33.6}Te_{62.5}$ films and the negligible difference between the atomic density and Debye temperature of $AgSbTe_2$ and Sb_2Te_3 ($3.11 \times 10^{28}\, m^{-3}$ and 200 K, respectively) but the large disparity in average sound speed (2900 ms^{-1} for Sb_2Te_3)[42,43], we use the latter as a fitting parameter for the data obtained after annealing $Ag_{3.9}Sb_{33.6}Te_{62.5}$ films at 68 °C, obtaining an intermediate result of 2400 ms^{-1}. The thermal conductivity of amorphous $Ag_{3.9}Sb_{33.6}Te_{62.5}$ needs to be reduced by 20% to match the experimental results, a behavior that has already been observed in other complex amorphous materials[39]. As the films become more crystalline upon annealing, the enhanced acoustic properties improve the thermal conductivity and increase its dependency on the temperature. In crystalline structures, Umklapp scattering dominates the phonon transport at the temperature range of interest, which shortens the phonon mean free path and leads to a reduction in the thermal conductivity with the temperature. The thermal conductivity of crystalline samples κ_C is computed using the Callaway model[44], which is expressed as

$$\kappa_C = \frac{k_B}{2\pi^2} \left(\frac{k_B T}{\hbar}\right)^3 \int_0^{\Theta_D/T} \tau \frac{x^4 e^x}{(e^x - 1)^2} dx, \tag{3}$$

where the average phonon relaxation time τ is computed combining phonon-grain boundary $\tau_{GB}^{-1} = \frac{v_g}{3D/4} \frac{1-p}{p}$, film boundaries $\tau_B^{-1} = \frac{v_g}{t}$, phonon-impurity $\tau_I^{-1} = A\omega^4$, Umklapp $\tau_U^{-1} = B\omega^2 T exp\left(-\frac{\Theta_D}{T}\right)$, phonon-carrier $\tau_C^{-1} = C\omega$, and, in the case of $Ag_{3.9}Sb_{33.6}Te_{62.5}$ films, nanoprecipitate $\tau_{NP}^{-1} = v_g \Theta n_{NP}$ scattering mechanisms as

$\tau^{-1} = \tau_{GB}^{-1} + \tau_B^{-1} + \tau_I^{-1} + \tau_U^{-1} + \tau_C^{-1} + \tau_{NP}^{-1}$[45–47], where D is the average grain size, P is the phonon transmission across the grain boundary, t is the thickness of the film, n_{NP} is the nanoprecipitate number density, and Θ is the average nanoprecipitate scattering cross-section, which is estimated using the average nanoinclusion size, and the mass and tensor strength difference with the matrix[17,48]. As detailed at the beginning of this section, the thickness of the film is measured using cross-sectional SEM imaging and the grain size is derived from the XRD spectra. The carrier scattering fitting parameter is taken as $C = 8.2 \times 10^{-5}$ [49] whereas the phonon-impurity and Umklapp scattering fitting parameters A and B are obtained from the best fit to our experimental data. We first find the impurity and Umklapp scattering parameters from Eq. (3) by fitting the data obtained after annealing at 133 °C and the amorphous phase from Eq. (2) by using the data obtained at the lowest annealing temperature; then, we find the crystalline fraction x that fits the data at the other temperatures. The fitting parameters result in $A_{AgSbTe_2} = 9.0 \cdot 10^{-41}\ s^3$, $A_{Ag_{3.9}Sb_{33.6}Te_{62.5}} = 8.5 \cdot 10^{-42}\ s^3$, $B_{AgSbTe_2} = 8.48 \cdot 10^{-15}\ s^{-3}$, and $B_{Ag_{3.9}Sb_{33.6}Te_{62.5}} = 1.32 \cdot 10^{-15}\ s^{-3}$. These results show stronger dependency in impurity scattering than the previously reported $Sb_{37}Te_{63}$ films[8,49]. However, we noticed that the thermal conductivity of the $Ag_{3.9}Sb_{33.6}Te_{62.5}$ films annealed below 133 °C cannot be fitted with such a strong impurity scattering component, and the best fitting results in $A_{Ag_{3.9}Sb_{33.6}Te_{62.5}} = 3.3 \cdot 10^{-43}\ s^3$ and $B_{Ag_{3.9}Sb_{33.6}Te_{62.5}} = 3.96 \cdot 10^{-15}\ s^{-3}$. This indicates that the $Ag_{3.9}Sb_{33.6}Te_{62.5}$ film might have started degradation when being annealed at 133 °C despite the SiO_2 encapsulation. Alternatively, the weaker temperature-dependency after annealing at 133 °C might be due to the contribution of the electron thermal conductivity, which has a positive temperature dependence that can neutralize the negative temperature dependence of the lattice thermal conductivity[23]. Furthermore, temperature-dependent data after annealing at 161 °C was not possible due to degradation of the films at that temperature that caused leaking of the applied current. All Umklapp fitting parameters are lower than those previously obtained for Sb_2Te_3 films[8] due to the stronger dependency on impurity scattering and the scattering by the nanoprecipitates. The coexistence of Sb_2Te_3 and β-Ag_2Te nanoprecipitates in $Ag_{3.9}Sb_{33.6}Te_{62.5}$ films does not produce a significant reduction in the thermal conductivity of the films due to the low volume fraction and similar thermal conductivity of both phases[50,51]. The results indicate that the crystalline fractions of the $Ag_{3.9}Sb_{33.6}Te_{62.5}$ films annealed at 110, 94 and 68 °C are 0.45, 0.18 and 0, respectively; while those of $AgSbTe_2$ films annealed at 94 and 68 °C are 0.1, 0.01, respectively. These crystalline fractions are lower than those previously obtained for $Sb_{37}Te_{63}$ films[8], which further indicates that the presence of silver inhibits the nucleation of Sb_2Te_3 and $AgSbTe_2$ crystals.

Conclusions

We find the room-temperature thermal conductivity of electrodeposited $AgSbTe_2$ thin films to be lower than that of the previously reported $Sb_{37}Te_{63}$ films[8] due to the impeded thermal transport resulted from the inhibited nucleation and growth of Sb_2Te_3 crystals. The room-temperature thermal conductivity of electrodeposited $Ag_{3.9}Sb_{33.6}Te_{62.5}$ films is lower that of $Sb_{37}Te_{63}$ films[8] when the pre-annealing temperature is below 110 °C, and there is no significant difference when the pre-annealing temperature is above 110 °C. By annealing at 160 °C, the room-temperature thermal conductivities of $Ag_{3.9}Sb_{33.6}Te_{62.5}$ and $AgSbTe_2$ films increase from 0.24 $Wm^{-1}K^{-1}$ to 1.59 $Wm^{-1}K^{-1}$ and from 0.17 $Wm^{-1}K^{-1}$ to and 0.56 $Wm^{-1}K^{-1}$, respectively. We estimate the zT of 0.95 for $Ag_{3.9}Sb_{33.6}Te_{62.5}$ and 0.93 for $AgSbTe_2$ after annealing at 100 °C for 30 minutes by using the measured thermal conductivity values (0.59 $Wm^{-1}K^{-1}$ for $Ag_{3.9}Sb_{33.6}Te_{62.5}$ and 0.22 $Wm^{-1}K^{-1}$ for $AgSbTe_2$) from this paper and the measured power factors (1870 $\mu Wm^{-1}K^{-2}$ for $Ag_{3.9}Sb_{33.6}Te_{62.5}$ and 553 $\mu Wm^{-1}K^{-2}$ for $AgSbTe_2$) from the previous publications[7,22], in which the samples were created from the same batch and treated with the same annealing conditions. The presented zT values at room are higher than any other $Ag_xSb_yTe_z$ films or nanostructures reported in the literature[11,26–29]. We attribute this to the unique phase control and the role of Ag in inhibiting nucleation.

The transient and temperature-dependent thermal conductivity measurements reveal that the silver content in $Ag_{3.9}Sb_{33.6}Te_{62.5}$ films delays the formation of Sb_2Te_3 crystals but has little impact on the thermal conductivity, which is different from the large impact observed on electrical properties[7,22]. Our work shows that electrodeposited antimony telluride thin films with proper annealing conditions can be excellent thermoelectric materials, and $AgSbTe_2$ is particularly promising due to the high crystallization activation energy and low thermal conductivity. These results improve our understanding of the role of metal content in chalcogenides for thermal transport and guide optimal designs of thermoelectric materials for near-room-temperature applications.

Methods

Amorphous $AgSbTe_2$ and $Ag_{3.9}Sb_{33.6}Te_{62.5}$ films are prepared using the established electrodeposition method as schematized in Fig. 1(a) [52–54]. The detailed process that allows well-controlled film composition by adjusting the applied potential and the electrolyte composition can be found in our previous publications[6,7,22]. After the amorphous $Ag_xSb_yTe_z$ thin films are deposited on SiO_2 (300 nm)/Ti (30 nm)/Au (50 nm) films on a Si substrate, we deposit a 150 nm SiO_2 layer by e-beam deposition to electrically passivate the films, and we fabricate the nickel electrodes required for the thermal conductivity measurements through photolithography patterning and electron beam evaporation of Cr (20 nm)/Ni (100 nm) films. The film temperature during all fabrication steps is limited to 50 °C to prevent any phase transition[6,7,22].

The 3ω method[8,25,36,55,56] is used to measure the cross-plane thermal conductivity. Briefly, in this method patterned metal lines, with a width ranging from 2 to 100 μm and a length ranging from 200 to 1000 μm, are used as both heaters and sensors. When an AC current (Keithley™ 6221 current source) at frequency ω causes Joule heating, it induces a temperature oscillation at 2ω, which results in a voltage drop across the heater at 3ω due to the metal characteristic electrical resistivity change with temperature[57]. The third harmonic of the voltage $V_{3\omega}$, which is recorded using a Stanford Research™ SR830 lock-in amplifier, is used to compute the temperature rise as $\Delta T = \frac{2V_{3\omega}}{V_{1\omega} TCR}$, where the temperature coefficient of resistance $\left(TCR = \frac{1}{R_0}\frac{dT}{dR}\right)$ is computed by the best fit to the measured resistance at different sample temperatures. The circuit used to measure the third harmonic is detailed

in Fig. S2. The lock-in amplifiers are phase- and frequency-locked to the current source to avoid measuring the grid noise. To avoid saturating the lock-in amplifier with the first harmonic, an operational amplifier circuit is used to cancel the first harmonic, which is read by the multimeter and generated by the second lock-in amplifier in phase and at the same frequency. The temperature rise with a given applied current depends on how the underlying materials dissipate the heat generated and, therefore, is used to fit a multilayer heat conduction solution that accounts for the thermal resistance of each film, substrate, and relevant interfaces[56]. In order to accurately capture the thermal conductivity and thermal boundary resistances of the other layers (SiO_2 and adhesion metal layers), we perform a differential measurement by measuring first the layer stack without the electrodeposited film. To identify the thermal conductivity variation with the film phase and crystallinity, the as-deposited amorphous $AgSbTe_2$ and $Ag_{3.9}Sb_{33.6}Te_{62.5}$ thin films are annealed at temperatures up to 160 °C for 30 minutes and then cooled down to room temperature to measure the thermal conductivity. The films then are heated on a hot plate using a Lake Shore™ 330 temperature controller in vacuum (Janis™ VPF-800) and a resistance temperature detector mounted on the chip holder provides an accurate temperature reading. Additionally, the formation kinetics of both materials is analyzed by annealing amorphous $AgSbTe_2$ and $Ag_{3.9}Sb_{33.6}Te_{62.5}$ films at 94 °C for 5.5 hours while measuring their thermal conductivity every 5 minutes with the 3ω method after the temperature of the sample stabilizes within 30 mK of the annealing temperature; and the heat transport mechanisms are studied using the temperature-dependent thermal conductivity after pre-annealing at different temperatures.

Data Availability

The datasets generated during and/or analyzed during the current study are available from the corresponding author on reasonable request.

References

1. Minnich, A. J., Dresselhaus, M. S., Ren, Z. F. & Chen, G. Bulk nanostructured thermoelectric materials: Current research and future prospects. *Energy Environ. Sci.* **2**, 466–479 (2009).
2. Heremans, J. P., Thrush, C. M. & Morelli, D. T. Thermopower enhancement in lead telluride nanostructures. *Phys. Rev. B - Condens. Matter Mater. Phys.* **70**, 115334 (2004).
3. Venkatasubramanian, R., Siivola, E., Colpitts, T. & O'Quinn, B. Thin-film thermoelectric devices with high room-temperature figures of merit. *Nature* **413**, 597–602 (2001).
4. Bux, S. K. *et al*. Nanostructured bulk silicon as an effective thermoelectric material. *Adv. Funct. Mater.* **19**, 2445–2452 (2009).
5. Zhao, L.-D. *et al*. Ultralow thermal conductivity and high thermoelectric figure of merit in SnSe crystals. *Nature* **508**, 373–377 (2014).
6. Kim, J. *et al*. Maximizing thermoelectric properties by nanoinclusion of γ-SbTe in Sb2Te3 film via solid-state phase transition from amorphous Sb-Te electrodeposits. *Nano Energy* **13**, 727–734 (2015).
7. Kim, J., Lee, K. H. K. H., Kim, S.-D. S.-D., Lim, J.-H. J. & Myung, N. V. N. V. Simple and effective fabrication of Sb2Te3 films embedded with Ag2Te nanoprecipitates for enhanced thermoelectric performance. *J. Mater. Chem. A* **6**, 349–356 (2018).
8. Yu, Z. *et al*. Phase-dependent thermal conductivity of electrodeposited antimony telluride films. *J. Mater. Chem. C* **6**, 3410–3416 (2018).
9. Pei, Y., Lensch-Falk, J., Toberer, E. S., Medlin, D. L. & Snyder, G. J. High thermoelectric performance in PbTe due to large nanoscale Ag 2Te precipitates and la doping. *Adv. Funct. Mater.* **21**, 241–249 (2011).
10. Liu, W. *et al*. Optimized thermoelectric properties of Sb-doped Mg2(1 + z)Si0.5- ySn0.5S by through adjustment of the Mg content. *Chem. Mater.* **23**, 5256–5263 (2011).
11. Du, B., Li, H., Xu, J., Tang, X. & Uher, C. Enhanced figure-of-merit in Se-doped p-type AgSbTe2 thermoelectric compound. *Chem. Mater.* **22**, 5521–5527 (2010).
12. Yamashita, O., Tomiyoshi, S. & Makita, K. Bismuth telluride compounds with high thermoelectric figures of merit. *J. Appl. Phys.* **93**, 368–74 (2003).
13. Mehta, R. J. *et al*. Seebeck and figure of merit enhancement in nanostructured antimony telluride by antisite defect suppression through sulfur doping. *Nano Lett.* **12**, 4523–452 (2012).
14. Hockings, E. F. The thermal conductivity of silver antimony telluride. *J. Phys. Chem. Solids* **10**, 341–342 (1959).
15. Lee, J. K. J. E. *et al*. Enhanced thermoelectric properties of AgSbTe2 obtained by controlling heterophases with Ce doping. *Sci. Rep.* **7**, 1–8 (2017).
16. Ma, J. *et al*. Glass-like phonon scattering from a spontaneous nanostructure in AgSbTe 2. *Nat. Nanotechnol.* **8**, 445–451 (2013).
17. Wang, Z. *et al*. Understanding phonon scattering by nanoprecipitates in potassium-doped lead chalcogenides. *ACS Appl. Mater. Interfaces* **9**, 3686–3693 (2017).
18. Mingo, N., Hauser, D., Kobayashi, N. P., Plissonnier, M. & Shakouri, A. Nanoparticle-in-alloy approach to efficient thermoelectrics: Silicides in SiGe. *Nano Lett.* **9**, 711–715 (2009).
19. Lee, M. H., Kim, K. R., Rhyee, J. S., Park, S. D. & Snyder, G. J. High thermoelectric figure-of-merit in Sb2Te3/Ag2Te bulk composites as Pb-free p-type thermoelectric materials. *J. Mater. Chem. C* **3**, 10494–10499 (2015).
20. Kim, S. I. S. W. *et al*. Dense dislocation arrays embedded in grain boundaries for high-performance bulk thermoelectrics. *Science.* **348**, 109–114 (2015).
21. Joshi, G. *et al*. Enhanced thermoelectric figure-of-merit in nanostructured p-type silicon germanium bulk alloys. *Nano Lett.* **8**, 4670–4674 (2008).
22. Kim, J., Lee, J.-Y. Y., Lim, J.-H. H. & Myung, N. V. Optimization of Thermoelectric Properties of p-type AgSbTe2 Thin Films via Electrochemical Synthesis. *Electrochim. Acta* **196**, 579–586 (2016).
23. Li, Q. *et al*. Temperature dependent thermal conductivity and transition mechanism in amorphous and crystalline Sb2Te3 thin films. *Sci. Rep.* **7**, 13747 (2017).
24. Morelli, D. T., Jovovic, V. & Heremans, J. P. Intrinsically minimal thermal conductivity in cubic I-V-VI2 semiconductors. *Phys. Rev. Lett.* **101**, 035901 (2008).
25. Lee, J. *et al*. Thermal conductivity anisotropy and grain structure in Ge2Sb2Te5 films. *J. Appl. Phys.* **109**, 084902 (2011).
26. Liu, W., Yan, X., Chen, G. & Ren, Z. Recent advances in thermoelectric nanocomposites. *Nano Energy* **1**, 42–56 (2012).
27. Zhu, T. *et al*. Compromise and Synergy in High-Efficiency Thermoelectric Materials. *Adv. Mater.* **29**, 1605884 (2017).
28. Xu, J. *et al*. High thermoelectric figure of merit and nanostructuring in bulk AgSbTe2. *J. Mater. Chem.* **20**, 6138 (2010).
29. Gao, W., Wang, Z., Huang, J. & Liu, Z. Extraordinary thermoelectric performance realized in hierarchically structured AgSbSe2 with ultralow thermal conductivity. *ACS Appl. Mater. Interfaces* **10**, 18685–18692 (2018).
30. Choy, C. L. Thermal conductivity of polymers. *Polymer (Guildf).* **18**, 984–1008 (1977).
31. Hasselman, D. P. H. & Johnson, L. F. Effective Thermal Conductivity of Composites with Interfacial Thermal Barrier Resistance. *J. Compos. Mater.* **21** (1987).

32. Nan, C.-W. W., Birringer, R., Clarke, D. R. & Gleiter, H. Effective thermal conductivity of particulate composites with interfacial thermal resistance. *J. Appl. Phys.* **81**, 6692 (1997).
33. Pietrak, K. & Winiewski, T. S. A review of models for effective thermal conductivity of composite materials. *J. J. Power Technol.* **95**, 14–24 (2015).
34. Benveniste, Y. Effective thermal conductivity of composites with a thermal contact resistance between the constituents: Nondilute case. *J. Appl. Phys.* **61**, 2840 (1987).
35. Every, A. G., Tzou, Y., Hasselman, D. P. H. & Raj, R. The effect of particle size on the thermal conductivity of ZnS/diamond composites. *Acta Metall. Mater.* **40**, 123–129 (1992).
36. Lee, J., Kodama, T., Won, Y., Asheghi, M. & Goodson, K. E. Phase purity and the thermoelectric properties of Ge2Sb2Te5films down to 25 nm thickness. *J. Appl. Phys.* **112**, 014902 (2012).
37. Ferrer-Argemi, L. *et al*. Size-dependent electrical and thermal conductivities of electro-mechanically-spun glassy carbon wires. *Carbon N. Y.* **130**, 87–93 (2018).
38. Ferrer-Argemi, L., Cisquella-Serra, A., Madou, M. & Lee, J. Temperature-Dependent Electrical and Thermal Conductivity of Glassy Carbon Wires. *Proc. 17th Intersoc. Conf. Therm. Thermomechanical Phenom. Electron. Syst. ITherm 2018* **1**, 1280–1288 (2018).
39. Cahill, D. G. & Pohl, R. O. Heat flow and lattice vibrations in glasses. *Solid State Commun.* **70**, 927–930 (1989).
40. Wojciechowski, K. & Schmidt, M. Structural and thermoelectric properties of AgSbTe2-AgSbSe2 pseudobinary system. *Phys. Rev. B* **79**, 184202 (2009).
41. Pereira, P. B. & Hermann, R. Structure and Lattice Dynamics of Thermoelectric Complex Chalcogenides. *Faculte Des Sciences* Docteur en, (University of Liege, 2012).
42. Chen, X. *et al*. Thermal expansion coefficients of Bi 2Se 3 and Sb 2Te 3 crystals from 10 K to 270 K. *Appl. Phys. Lett.* **99**, 261912 (2011).
43. Bessas, D. *et al*. Lattice dynamics in Bi2Te3 and Sb2Te 3: Te and Sb density of phonon states. *Phys. Rev. B - Condens. Matter Mater. Phys.* **86**, 224301 (2012).
44. Callaway, J. Model for lattice Thermal Conductivity at Low Temperatures. *Phys. Rev.* **113**, 1046–1051 (1959).
45. Lee, J. *et al*. Thermal Transport in Silicon Nanowires at High Temperature up to 700 K. *Nano Lett.* **16**, 4133–4140 (2016).
46. Yu, Z., Ferrer-Argemi, L. & Lee, J. Investigation of thermal conduction in symmetric and asymmetric nanoporous structures. *J. Appl. Phys.* **122**, 244305 (2017).
47. Ren, Z. & Lee, J. Thermal conductivity anisotropy in holey silicon nanostructures and its impact on thermoelectric cooling. *Nanotechnology* **29**, 045404 (2018).
48. Cahill, D. G. *et al*. Nanoscale thermal transport. II. 2003–2012. *Appl. Phys. Rev.* **1**, 011305 (2014).
49. Lošťák, P. *et al*. Transport coefficients and defect structure of Sb2-xAgxTe3 single crystals. *J. Phys. Chem. Solids* **67**, 1457–1463 (2006).
50. Taylor, P. F. & Wood, C. Thermoelectric properties of Ag2Te. *J. Appl. Phys.* **32**, 1–3 (1961).
51. Saci, A., Battaglia, J.-L., Kusiak, A., Fallica, R. & Longo, M. Thermal conductivity measurement of a Sb2Te3 phase change nanowire. *Appl. Phys. Lett.* **104**, 263103 (2014).
52. Jung, H. & Myung, N. V. Electrodeposition of antimony telluride thin films from acidic nitrate-tartrate baths. *Electrochim. Acta* **56**, 5611–5615 (2011).
53. Lim, J. H. *et al*. Electrodeposition of p-type Sb x Te y thermoelectric films. *J. Electron. Mater.* **40**, 1321–1325 (2011).
54. Song, Y. *et al*. Electrodeposition of thermoelectric Bi2Te3thin films with added surfactant. *Curr. Appl. Phys.* **15**, 261–264 (2015).
55. Cahill, D. G. Thermal conductivity measurement from 30 to 750 K: The 3?? method. *Rev. Sci. Instrum.* **61**, 802–808 (1990).
56. Kim, J. H., Feldman, A. & Novotny, D. Application of the three omega thermal conductivity measurement method to a film on a substrate of finite thickness. *J. Appl. Phys.* **86**, 3959–3963 (1999).
57. Yu, Z., Ferrer-argemi, L. & Lee, J. Temperature-dependent Thermoelectric Properties of Electrodeposited Antimony Telluride Films upon Thermal Annealing. *2018 17th IEEE Intersoc. Conf. Therm. Thermomechanical Phenom. Electron. Syst.* 227–234 (2018).

Acknowledgements

This research was supported by startup funds from the Samueli School of Engineering at UCI and by the Global Frontier Program through the Global Frontier Hybrid Interface Materials (GFHIM) project of the National Research Foundation of Korea (NRF), funded by the Ministry of Science, ICT, & Future Planning (2013M3A6B1078870). N.V. Myung would like to acknowledge support by Future Materials Discovery Program through the NRF funded by the Ministry of Science, ICT & Future Planning (NRF-2016M3D1A1027836).

Author Contributions

L.F.-A., Z.Y. and J.L. wrote the manuscript. L.F.-A. took the SEM images and prepared the figures. J.K. prepared the films. Z.Y. fabricated the electrodes. L.F.-A. and Z.Y. performed the thermal conductivity measurements. L.F.-A. did the film characterization. N.V.M., J.-H.L. and J.L. advised and gave valuable suggestions. All authors reviewed the manuscript.

Additional Information

Supplementary information accompanies this paper at https://doi.org/10.1038/s41598-019-45697-9.

Competing Interests: The authors declare no competing interests.

Publisher's note: Springer Nature remains neutral with regard to jurisdictional claims in published maps and institutional affiliations.

Open Access This article is licensed under a Creative Commons Attribution 4.0 International License, which permits use, sharing, adaptation, distribution and reproduction in any medium or format, as long as you give appropriate credit to the original author(s) and the source, provide a link to the Creative Commons license, and indicate if changes were made. The images or other third party material in this article are included in the article's Creative Commons license, unless indicated otherwise in a credit line to the material. If material is not included in the article's Creative Commons license and your intended use is not permitted by statutory regulation or exceeds the permitted use, you will need to obtain permission directly from the copyright holder. To view a copy of this license, visit http://creativecommons.org/licenses/by/4.0/.

© The Author(s) 2019